

Article

Not peer-reviewed version

---

# Atomistic Modelling of Spinel Oxide Particle Shapes and Reshaping under OER Conditions

---

Öyküm Naz Avcı , [Luca Sementa](#) <sup>\*</sup> , [Alessandro Fortunelli](#) <sup>\*</sup>

Posted Date: 27 December 2023

doi: 10.20944/preprints202312.0145.v2

Keywords: oxygen evolution reaction; Density Functional Theory; reaction mechanisms; spinel oxides



Preprints.org is a free multidiscipline platform providing preprint service that is dedicated to making early versions of research outputs permanently available and citable. Preprints posted at Preprints.org appear in Web of Science, Crossref, Google Scholar, Scilit, Europe PMC.

Copyright: This is an open access article distributed under the Creative Commons Attribution License which permits unrestricted use, distribution, and reproduction in any medium, provided the original work is properly cited.

Article

# Atomistic Modelling of Spinel Oxide Particle Shapes and Reshaping under OER Conditions

Öyküm N. Avcı<sup>1,2</sup>, Luca Sementa<sup>3,\*</sup> and Alessandro Fortunelli<sup>1,\*</sup>

<sup>1</sup> CNR-ICCOM, Consiglio Nazionale delle Ricerche, via G. Moruzzi 1, 56124, Pisa, Italy;

<sup>2</sup> Department of Chemistry and Industrial Chemistry, DSCM, University of Pisa, Via G. Moruzzi 13, Pisa, Italy;

<sup>3</sup> CNR- IPCF, Istituto per i Processi Chimico-Fisici, Via G. Moruzzi 1, 56124, Pisa, Italy;

\* Correspondence: [alessandro.fortunelli@cnr.it](mailto:alessandro.fortunelli@cnr.it) (AF), [luca.sementa@cnr.it](mailto:luca.sementa@cnr.it) (LS)

**Abstract:** The surface configurations of the low-index facets of a set of spinel oxides are investigated using DFT+U calculations to derive surface energies and predict equilibrium nanoparticle shapes via the Wulff construction. Two very different conditions are investigated, corresponding to application either in heterogeneous catalysis or in electrocatalysis. First, the bare stoichiometric surfaces of NiFe<sub>2</sub>O<sub>4</sub>, CoFe<sub>2</sub>O<sub>4</sub>, NiCo<sub>2</sub>O<sub>4</sub>, ZnCo<sub>2</sub>O<sub>4</sub> spinels are studied to model their use as high-temperature oxidation catalysts. Second, focusing attention on the electrochemical oxygen evolution reaction (OER), and on the CoFe<sub>2</sub>O<sub>4</sub> inverse spinel as the most promising OER catalyst, we generate surface configurations by adsorbing OER intermediates, and, in an innovative study, we recalculate surface energies taking into account adsorption and environmental conditions, i.e., applied electrode potential and O<sub>2</sub> pressure. We predict that, under OER operating conditions, (111) facets are dominant in CoFe<sub>2</sub>O<sub>4</sub> nanoparticle shapes, in fair agreement with microscopy measurements. Importantly, in the OER case we predict a strong dependence of nanoparticle shape upon O<sub>2</sub> pressure. Increasing O<sub>2</sub> pressure increases the size of the higher-index (111) and (110) facets at the expense of the (001) more catalytically active facet, whereas the opposite occurs at low O<sub>2</sub> pressure. These predictions should be experimentally verifiable and help define the optimal OER operative conditions.

**Keywords:** oxygen evolution reaction; DFT; reaction mechanism; electrocatalysis; spinel oxides; Ni-Fe oxides; Co-Fe oxides

## 1. Introduction

Nanomaterials, such as metal or metal oxide nanoparticle systems, find applications in many areas of technology, such as biomedical, sensors, optics, storage and energy harvesting materials, as well as in heterogeneous catalysis, where they play a dominant role [1]. Their function is closely linked to their structure in terms of nanoparticle size and shape [2]. Therefore, controlling the shape of metal or metal oxide nanoparticles is one of the major challenges in applications, as this has a dramatic effect on material properties, e.g., determining number and type and performance of active sites in catalysis.

The shapes of nanoparticles can be determined via the Wulff construction, proposed by the mineralogist George Wulff at the beginning of the twentieth century [3]. This method was used in geology, mineralogy and crystallography, and was then rediscovered in materials science to predict the shapes of nanoparticles. The Wulff construction allows one to predict the nanoparticle shape through knowledge of their surface energies, data which can be and have been calculated for many systems via e.g. theoretical simulations based on first-principles quantum-mechanical methods [1]. Some characteristic equilibrium shapes often found in materials with cubic symmetry are shown in Figure 1.



Figure 1. Examples of Wulff constructions for shapes of high cubic symmetry.

Following the fundamental work by Gibbs [4], and introducing the principle of minimum surface free energy to determine the shape of a crystal at equilibrium, Wulff proposed [3] that the shape of a crystalline material to be constructed via the following recipe:

$$\frac{\gamma_{hkl(n)}}{r_{hkl}} = \text{constant}, \quad \forall hkl \quad (1)$$

where  $\gamma_{hkl}$  is the energy required to create a surface of unit area normal to the  $(hkl)$  vector, and  $r_{hkl}$  is the distance from the center of the crystal to the  $hkl$  plane. This process is repeated for all sets of Miller indexes,  $hkl$ , uniquely identifying a surface. The ratio of the surface energy,  $\gamma_{hkl}$ , to the distance from the center of the crystal,  $r_{hkl}$ , to any plane is constant in the Wulff construction.

In heterogeneous catalysis by metal nanoparticles, the catalytic functionality is strongly linked to their shape, especially for structure-sensitive reactions, which makes predictions of their morphology via e.g. computational methods an important goal. For example, Nørskov et al. obtained the equilibrium polyhedron shape of Ru nanoparticles, estimated the catalytic rates by summing contributions of the various facets, and compared with experimental measurements of transmission electron microscopy (TEM) and catalytic rates, finding reasonable agreement with experiment [5]. Vilé *et al.* investigated supported Ag catalyst nanoparticles (2-20 nm in diameter) to determine active sites for the olefin reaction using the atomistic Wulff construction and reported that the nanoparticles have the highest density of B5 sites, which are the active centers in the reaction [6]. Larger nanoparticles may expose higher-index facets: Wulff shapes of large Au nanoparticles were predicted to include (332), (001), (111), (211), and (322) facets, whereas nanoparticles smaller than 16 nm in diameter expose only (111) and (001) facets [7]. However, the equilibrium shape rarely contains facets with indexes higher than (001), (111), (110): high-index surfaces have a higher surface tension, and even if a high-index surface and a low-index surface have equal surface tensions, the low-index face will have a larger area as the high-index face will be steeper and be hidden in the Wulff construction [1].

Bare metal oxide facets have also been considered. In a systematic study, the surface structure, energies and morphology of bare cubic cobalt spinel nanocrystals with the formula  $M[\text{CoM}']\text{O}_4$  ( $M = \text{Mg, Zn, Fe, Co}$  and  $M' = \text{Ni, Al, Mn, Co}$ ) were investigated via Density-Functional Theory plus Hubbard correction (DFT+U) calculations, and compared directly with TEM and STEM experiments [8]. The authors predicted that the abundance of the (110) faces is always low (below 9%) and the surface energies typically increase in the sequence  $\gamma_{100} < \gamma_{111} < \gamma_{110}$  for cobalt spinel nanocrystals.

Computational studies of bare metal or metal oxide nanoparticles are appropriate for modeling high-temperature and low-coverage conditions. At high temperatures and low pressures, there is an entropic driving force for adsorbate species to leave the surface for the gas phase, giving rise to a low-coverage régime. These are the conditions of thermal catalysis, such as those occurring in oxidation processes: chemical looping, water gas shift reaction [9], methanol [10] and propanol [11] oxidation,  $\text{H}_2$  production [12], etc.

For nanoparticles under lower temperature and therefore higher-coverage conditions, instead, the influence of the chemical environment should be included in the Wulff construction by rescaling surface energies with adsorption energies [13]. For example, Au nanoparticles exposed to CO were found to be more spherical and more reactive compared to Au nanoparticles in a non-interacting

environments, in agreement with experimental data [7] and also in agreement with previous studies investigating the shape and chemical ordering upon CO and H adsorption of mono- and bi-metallic explicit atomistic nanoparticle models, thus going beyond the ideal Wulff construction [14]. Similarly, the surface free energies of MgO low-index crystal facets were investigated as a function of the temperature and water pressure through density functional theory, also comparing predictions with experimental observations [15]. It was predicted that (110) is a transient facet, and that the equilibrium Wulff shape of MgO crystals only involves (001) and (111) facets. Additionally, experiment and theory agreed on the pattern of the hydroxylated surface energies as  $\gamma_{111} < \gamma_{100} < \gamma_{110}$ , supporting the partial dissociation of water on MgO(001).

At the next level of complexity, the important question is how Wulff shape changes *under reaction conditions*, and how to account for this phenomenon at the theoretical level [16, 17]. There are a few examples of this research in thermal catalysis. In a pioneering study, the size- and corresponding morphology-dependent theoretical activity and selectivity of silver nanoparticles between 9 and 23 nm in diameter for the partial oxidation of propylene and the evolution of these quantities along the progress of the reaction were experimentally measured and compared with theoretical predictions based on the Wulff construction and explicit reaction mechanisms, finding an excellent agreement with experimental observations of evolution of the aspect ratio [16]. More recently, the concept of dynamical Wulff construction was explicitly introduced to account for particle reshaping under reaction conditions and employed to predict the shape of Si-doped iron nanoparticles during ammonia synthesis [17].

All this previous work refer to *thermal catalysis*. In contrast, application of Wulff-based theoretical protocols in the field of *electro-catalysis* is to the best of our knowledge lacking, despite the ever growing interest of the scientific and technological communities in this field [18,19]. In particular, the oxygen evolution reaction (OER) in Anion Exchange Membrane Water Electrolysis (AEMWE, or water splitting) represents a critical step in the realization of a sustainable hydrogen production whence a global hydrogen economy would arise, so that discovering and optimizing active and non-critical-material OER catalysts is one of the major challenges to XXI century chemistry.

Here, we address and fill this lack of knowledge in electro-catalysis by investigating for the first time spinel-type oxides via theoretical atomistic Wulff construction in a wide range of OER electro-catalytic conditions. Note that spinel-like iron-based spinels are promising OER electro-catalysts [20] due to their significant electrical conductivity, structural stability and catalytic performance, stemming from multiple valence of the cations and the ability to switch among different oxidation states [21,22]. We predict via first-principles DFT+U the surface energies of the most abundant (001), (110), and (111) facets of selected spinel oxide structures. To provide an exhaustive ensemble of data, we derive the equilibrium atomistic Wulff shapes of the corresponding nanoparticles under two very different sets of conditions:

- i) NiFe<sub>2</sub>O<sub>4</sub>, CoFe<sub>2</sub>O<sub>4</sub>, NiCo<sub>2</sub>O<sub>4</sub> and ZnCo<sub>2</sub>O<sub>4</sub> (inverse or normal) spinels as bare stoichiometric but non-symmetric surfaces to be compared with previous studies [8] and with characterization experiments and catalytic investigations under high-temperature, low-coverage conditions, such as those occurring in heterogeneous thermal catalysis [20];
- ii) the CoFe<sub>2</sub>O<sub>4</sub> inverse spinel, the most promising OER catalyst [23], for which we consider an extensive set of surface configurations with various coverage of adsorbate intermediates relevant during the electrochemical OER (H, OH, H<sub>2</sub>O, O, O<sub>2</sub>).

For the OER case, we also explore a wide set of environmental variables (applied electrode potential and O<sub>2</sub> pressure), so as to determine Wulff reshaping *under different OER conditions*, then finally comparing our predictions with available experimental characterization.

In case (i), in agreement with experiment and a previous systematic study [8], we predict that under high-temperature, low-coverage conditions (100) typically dominate.

In case (ii), also in agreement with experiment, we find that the most abundant CoFe<sub>2</sub>O<sub>4</sub> facets change from (100) for *bare* particles to (111) *under OER conditions*. Moreover, importantly, in the CoFe<sub>2</sub>O<sub>4</sub> OER case we find a strong phenomenon of nanoparticle reshaping upon O<sub>2</sub> pressure: increasing O<sub>2</sub> pressure reshapes the catalyst, increasing the size of the higher-index facets, *i.e.*, (111)

and (110), at the expense of the (001) facet, whereas the opposite occurs at low  $O_2$  pressure. Given that the OER catalytic activity of  $CoFe_2O_4$  spinels depends upon exposure of different facets [24-26], these predictions should be experimentally verifiable and help defining the optimal operative conditions for OER catalysis (and also oxidative catalysis), with potential implications, *e.g.*, on the design of OER electro-catalysts fulfilling societal requirement on activity, selectivity, efficiency, and cost.

## 2. Materials and Methods

Spin-polarized density functional theory plus Hubbard correction (DFT+U [27]) calculations were performed using a plane wave and ultrasoft pseudopotential framework [28] as implemented in the Quantum-Espresso [29] suite of codes. The Perdew-Burke-Ernzerhof (PBE) [30] exchange-correlation functional was used as DFT, augmented with Hubbard U parameters chosen as 3.3, 5.5, 3.0, 2.0 eV for Fe, Ni, Co, and Zn, respectively. It should be noted that we use an  $U_{\text{eff}}$  value of 3.0 eV for all type Co atoms (*i.e.*, octahedrally or/and tetrahedrally coordinated, depending on spinel type) to be consistent with a previous systematic theoretical study by Selloni *et al.* [31-33]. In our previous study [23], we used a value for  $U_{\text{eff}}$  of 4.5 eV as optimal for describing iron-based inverse spinels, in which cobalt only occupies an octahedral coordination. However, we verified that there is no significant difference between the two  $U_{\text{eff}}$  values in terms of configuration energetics. Kinetic energy cutoffs of 40 and 200 Ry were chosen for describing the wave function and the charge density, respectively. A  $3 \times 3 \times 1$  Monkhorst-Pack k-point mesh was utilized for energy and structural calculations. The WulffPack package was used to predict theoretical equilibrium shapes [34].

Spinel has general chemical formula  $AB_2X_4$  where  $A^{II}$  is a divalent cation like Mg, Cr, Mn, Fe, Co, Ni, Cu, Zn, Cd, Sn, and  $B^{III}$  is a trivalent cation like Al, Ga, In, Ti, V, Cr, Mn, Fe, Fe, Co, Ni, and X as O, S, Se *etc.* A normal spinel can be represented as:  $(A^{II})_{\text{tet}}(B^{III})_2\text{oct}O_4$ , whereas an inverse spinel can be represented as:  $(B^{III})_{\text{tet}}(A^{II})_{\text{oct}}(B^{III})_{\text{oct}}O_4$ , where the superscript "tet" and "oct" refer to tetrahedral and octahedral sites. The selected catalysts with inverse spinel structure ( $NiFe_2O_4$ ,  $CoFe_2O_4$  and  $NiCo_2O_4$ ) are ferrimagnetic [34], *i.e.*, they exhibit a spin arrangement:  $\uparrow\downarrow\uparrow$  for A(Oh)/B(Td)/B(Oh), using the notation: (A=Ni,Co; B=Fe,Co), spin up ( $\uparrow$ ), spin down ( $\downarrow$ ), and Oh and Td refer to octahedral and tetrahedral sites, respectively. At variance,  $ZnCo_2O_4$  only exists in the normal spinel structure and is ferromagnetic [35, 36], with spin arrangement:  $\uparrow\uparrow$  for A(Td)/B(Oh), where (A=Zn; B=Co). We verified that our DFT+U predictions are consistent with these expectations.

For the surface energy calculations under vacuum, corresponding to low-coverage thermal catalysis, the stoichiometric/non-symmetric slabs utilized for the three considered facets [(001), (110), (111)], including dipole correction, for inverse and normal spinel slab models are shown in Figure 2 and Figure 3.

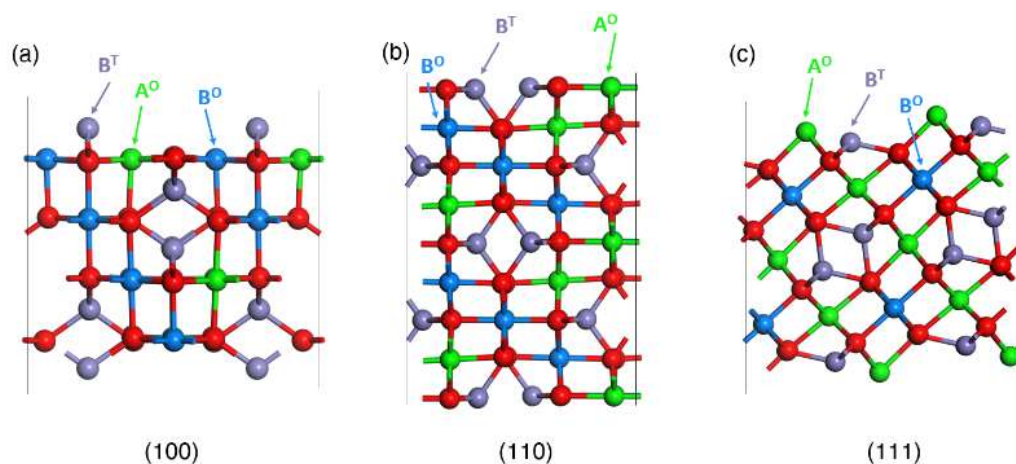


**Figure 2.** Stoichiometric but non-symmetric surface slab models for the considered surface terminations of inverse spinel ( $AB_2O_4$ ) systems in the ball and stick representation: (100) (a), (110) (b),

(111) (c). O and T denote octahedral and tetrahedral coordination of A and B metals, respectively. Conditions of thermal catalysis.

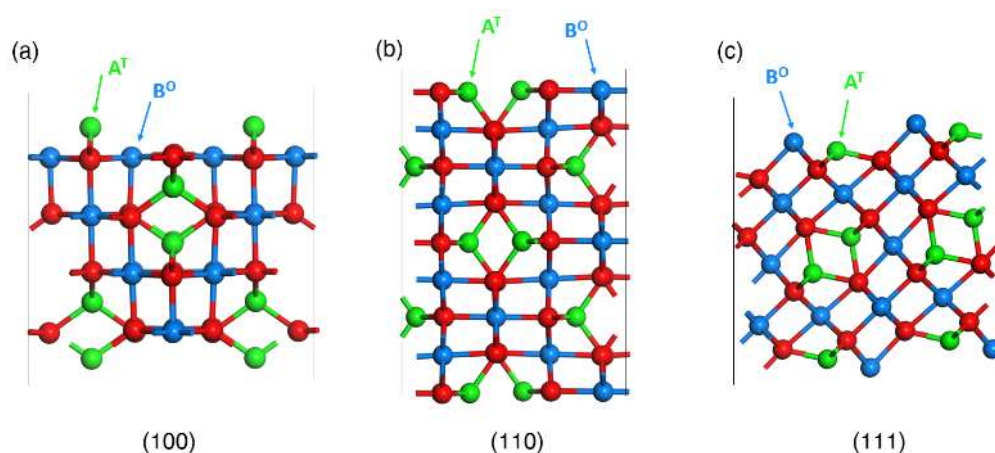


**Figure 3.** Stoichiometric but non-symmetric surface slab models for the considered surface terminations of normal spinel (AB<sub>2</sub>O<sub>4</sub>) systems in the ball and stick representation: (100) (a), (110) (b), (111) (c). T and O denote tetrahedral and octahedral coordination of A and B metals, respectively. Conditions of thermal catalysis.

For the (001) orientation, our model corresponds to a total of 56 atoms per unit cell for a thickness of 9 layers. For the (110) orientation, our slab with a thickness of 9 layers contains 126 atoms per unit cell, while for the (111) orientation our 9-layer thick unit cell contains 112 atoms. Note that there are two types of possible terminations for the (110) spinel orientation, which are usually labeled A and B in the literature [8, 37]. As the 110-A termination was reported to be more stable than the 110-B one in previous work [38], the latter was excluded from our analysis. Therefore, the (110) label only refers to the most stable (110)-A termination in this study.

We use Eq.(2) to calculate surface energies from optimized energies of bare slab models:

$$E_{surf}^{bare} = \frac{E(\text{slab of } n \text{ formula unit}) - nE(\text{bulk of 1 formula unit})}{2A} \quad (2)$$

The lattice parameters  $a, b, c$  of each stoichiometric slab have been derived after implementing variable-cell (vc) relaxation on the bulk phases of the investigated spinels, and are shown in Table S1 of the Supporting Information (SI).

We use the bulk optimized lattice parameters also to build non-stoichiometric/symmetric inverse spinel models for the high-coverage, i.e., electrochemical conditions, to investigate surfaces with various coverage of adsorbed OER intermediates on CoFe<sub>2</sub>O<sub>4</sub>. Non-stoichiometric but symmetric slab unit cells with dimensions of 5.99 Å × 5.99 Å × 25 Å for (001), 5.99 Å × 8.48 Å × 25 Å for (110), and 5.99 Å × 5.19 Å × 25 Å for (111) of inverse spinel slabs were built as shown in Figure 4.

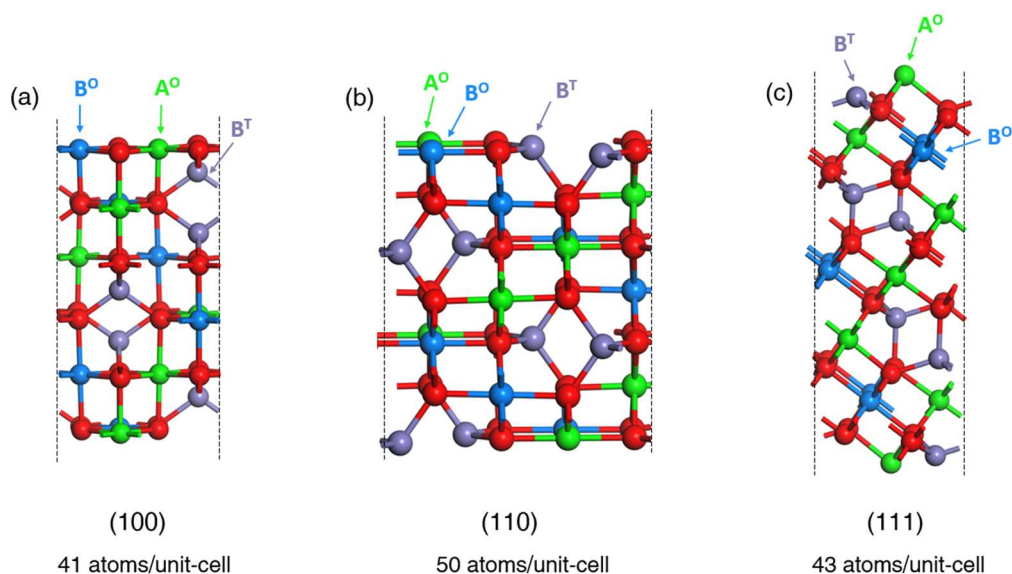


**Figure 4.** Non-stoichiometric/symmetric slab models for the considered surface terminations of inverse spinel systems in the ball and stick representation: (a) (001), (b) (110), (c) (111). O and T denote octahedral and tetrahedral coordination of A(Co) and B(Fe) metals, respectively. Conditions of electro-catalysis.

The total number of atoms per unit cell for (001), (110), (111) slabs used in bare and adsorbed surface calculations is summarized in Table S2 of the SI, and brief details about comparison of those slabs are shown in Figure S1.

To calculate surface energies for surfaces with adsorbates, we re-scale them as shown in Eq.(3), where adsorption energies are taken from optimization calculations of non-stoichiometric slab models [39]:

$$E_{surf}^{ads} = E_{surf}^{bare} + \frac{E_{ads}}{Area} \quad (3)$$

In the surfaces covered with oxygen, hydrogen and water, it is necessary to include entropy terms in the chemical potentials of these species, to obtain the system free energy ( $G$ ). Free energies are calculated using the same scheme utilized in previous studies [40, 41] and explained in detail in our previous work [23]. The total energy ( $E$ ) of each configuration was obtained directly via DFT. The contributions ( $\Delta H$ ,  $\Delta ZPE$ ,  $T\Delta S$ ) to the free energies ( $\Delta G$ ) of small molecules ( $H_2O$ , hydrogen and oxygen) were added empirically as:  $\Delta G_i = \Delta E_i + \Delta H_i + \Delta ZPE_i - T\Delta S_i$  [41], where standard thermodynamic data [42] are used to obtain the T and P contributions to the G values of aqueous  $H_2O$  and gaseous  $H_2$ .

The standard hydrogen electrode electrochemistry model [43] was finally used to calculate how the configuration energies depend upon the applied bias  $U$  via the proton-electron ( $H^+ + e^-$ ) transfer steps. In this approach, the standard hydrogen electrode (SHE) is used as a reference, so the proton ( $G[H^+]$ ) and electron ( $G[e^-]$ ) free energies are replaced by  $\frac{1}{2} G[H_2] - |e| U$ , where  $G[H_2]$  is the free energy of  $H_2$  and  $U$  is the electrode potential versus SHE. To get rid of the dependence of the applied potential upon pH, a reversible hydrogen electrode (RHE) reference is employed, so that the equilibrium potential required for OER is always 1.23 V vs. RHE at all pH values [44]. In other words, in calculating the over-potential, the pH term is canceled by taking the difference between predicted onset potentials and the equilibrium OER potential [45].

### 3. Results & Discussion

As anticipated in the Introduction, we divide our study into two parts. First, we focus on  $NiFe_2O_4$ ,  $CoFe_2O_4$ ,  $NiCo_2O_4$  and  $ZnCo_2O_4$  systems as *bare* stoichiometric surfaces: this corresponds to experiments at high temperature and low coverage, i.e., under the conditions of thermal heterogeneous catalysis [9-12]. This will allow us also to compare our predictions with and validate

against previous studies [8] (Section 3.1). Then, we switch to the most innovative part of our investigation, i.e. the Wulff construction under electrochemical OER conditions, and in Section 3.2 we consider the  $\text{CoFe}_2\text{O}_4$  system and study configurations with various coverage of (H, OH,  $\text{H}_2\text{O}$ , O,  $\text{O}_2$ ) adsorbate species under electrochemical OER and varying environmental variables (applied electrode potential,  $\text{O}_2$  pressure), so as to be able to make predictions on the optimal experimental conditions for OER [20].

### 3.1. Wulff Shapes of Bare Spinel Surfaces as Heterogenous Catalysts

For each investigated spinel: the  $\text{NiFe}_2\text{O}_4$ ,  $\text{CoFe}_2\text{O}_4$ ,  $\text{NiCo}_2\text{O}_4$  and  $\text{ZnCo}_2\text{O}_4$  oxides, stoichiometric ( $\text{AB}_2\text{O}_4$ ) but non-symmetric surface slab models were constructed for all considered terminations as shown in **Figure 2** and **Figure 3**. In the case of inverse spinels:  $\text{NiFe}_2\text{O}_4$ ,  $\text{CoFe}_2\text{O}_4$  and  $\text{NiCo}_2\text{O}_4$ ,  $\text{A}^{++}$  (M= Ni, Co) cations occupy octahedral sites and  $\text{B}^{3+}$  (M=Fe, Co) cations occupy both octahedral and tetrahedral sites. For the normal spinel  $\text{ZnCo}_2\text{O}_4$ ,  $\text{A}^{++}$  (M= Zn) cations occupy tetrahedral sites and  $\text{B}^{3+}$  cations (M=Co) occupy octahedral sites. Protruding cations on tetrahedral sides ( $\text{B}^{\text{T}}$  and  $\text{A}^{\text{T}}$ ) on top and bottom surface in (001) plane were retained to maintain the stoichiometry in both inverse and normal spinels.

After imposing the lattice parameters derived from variable-cell (vc) relaxation of the bulk, slab models were constructed, Cartesian coordinates were relaxed, and surface energies (in  $\text{J}/\text{m}^2$ ) of each facets were calculated using Eq.(2) and reported in **Figure 5** (top).

| DFT Surface Energies in $\text{J}/\text{m}^2$ |                           |                           |                           |                           |
|---|---------------------------|---------------------------|---------------------------|---------------------------|
| Facets  | $\text{NiFe}_2\text{O}_4$ | $\text{CoFe}_2\text{O}_4$ | $\text{NiCo}_2\text{O}_4$ | $\text{ZnCo}_2\text{O}_4$ |
| (001)   | 1.13                      | 1.06                      | 0.96                      | 0.52                      |
| (110)   | 1.74                      | 1.48                      | 1.28                      | 0.75                      |
| (111)   | 1.47                      | 1.37                      | 1.20                      | 0.98                      |

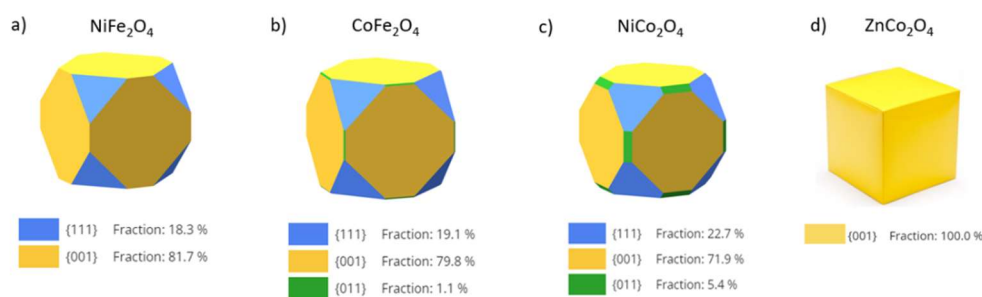


**Figure 5.** (Top) Calculated DFT Surface Energies ( $\text{J}/\text{m}^2$ ) for bare surfaces of selected spinel oxide structures. (Bottom) Calculated Wulff nanoparticle shapes of: (a)  $\text{NiFe}_2\text{O}_4$ , (b)  $\text{CoFe}_2\text{O}_4$ , (c)  $\text{NiCo}_2\text{O}_4$ , (d)  $\text{ZnCo}_2\text{O}_4$  based on optimized bare slab surfaces. Conditions of thermal catalysis.

As apparent from **Figure 5** (top), the calculated surface energies increase in the sequence  $\gamma_{001} < \gamma_{111} < \gamma_{110}$  for the three inverse spinels ( $\text{NiFe}_2\text{O}_4$ ,  $\text{CoFe}_2\text{O}_4$  and  $\text{NiCo}_2\text{O}_4$ ). We thus expect the (001) facets to have a larger extension since they exhibit the lowest surface energy in all cases. For the normal spinel  $\text{ZnCo}_2\text{O}_4$ , the sequence changes to:  $\gamma_{100} < \gamma_{110} < \gamma_{111}$ . However, the (001) facet is still expected to be dominant, actually up to the point of being unique, whence a predicted cubic equilibrium shape for  $\text{ZnCo}_2\text{O}_4$ .

By using surface energies as calculated above, the predicted equilibrium Wulff configurations of nanoparticle structures were modeled, and schematically depicted in **Figure 5** (bottom): Fe-based spinels,  $\text{NiFe}_2\text{O}_4$  and  $\text{CoFe}_2\text{O}_4$ , are shown in **Figure 5a** and **5b**, respectively, while Co-based spinels,  $\text{NiCo}_2\text{O}_4$  and  $\text{ZnCo}_2\text{O}_4$ , are shown in **Figure 5c** and **5d**, respectively. For  $\text{NiFe}_2\text{O}_4$ , the predicted Wulff shape consist of (001) facets with a fraction of 81.7% and of (111) facets with a fraction of 18.3%, while for  $\text{CoFe}_2\text{O}_4$  we find a little fraction of (110) (1.1%) as well, together with 19.1% fraction of (111) and a bigger fraction of (001) (79.8%). For Co-based spinels, the Wulff shape of  $\text{NiCo}_2\text{O}_4$  exhibits all three

facets with fraction of 71.9%, 22.7% and 5.4% for (001), (111) and (110) facets, respectively, whereas in contrast, the Wulff shape of the normal spinel  $\text{ZnCo}_2\text{O}_4$  has a pure cube shape without any inclusion of (111) or (110) facets.

As discussed in the introduction, the modelling of spinel surfaces as bare so far refers to low-pressure(vacuum)/low-coverage/high-temperature conditions. In the study of Zasada et al. [8], the authors employed an analogous approach based on periodic DFT+U calculations for a different set of spinel oxide materials and compared their predictions with the results of TEM/STEM experiments on bare nanoparticles. Similar to the present study, the three most stable, (001), (110), and (111), planes exposed by mixed cobalt spinel nanocrystals were investigated [8]. In their findings, the abundance of the (110) faces is always low (below 9%) regardless of the nature of the secondary metal in the mixed cobalt spinels. These predictions match very well our findings predicting a very low abundance of (110) facets in the Wulff nanoparticle shapes, and the fact that the (001) facet dominates all investigated spinels with a high abundance (>70%). Our predictions should set the ground for a detailed study of the activity of these different materials and their surfaces in heterogeneous catalysis [9-12, 20].

### 3.2. Wulff Shapes of Spinel Surfaces under Electrochemical Conditions

In Section 3.1 we have not included the effects of reaction conditions and of chemical environment on spinel oxide nanoparticle shapes. Rescaling of surface energies must be considered to get Wulff nanoparticle shapes under operative electrochemical conditions, on which we focus in this subsection. Therefore, we investigate OH,  $\text{H}_2\text{O}$ , and  $\text{O}_2$  adsorption on (001), (110) and (111) facets of  $\text{CoFe}_2\text{O}_4$ , we predict Wulff reshaping of  $\text{CoFe}_2\text{O}_4$  nanoparticles under OER electrochemical conditions, and we compare with experimental microscopy observations.

$\text{CoFe}_2\text{O}_4$  is selected to investigate the change of nanoparticle shape under OER conditions because of its higher OER performance [23]. For example, Li *et al.* prepared various inverse spinel  $\text{MFe}_2\text{O}_4$  (M = Co, Ni, Cu, and Mn) nanofibers by the electrospinning technique [46], and found that the OER performance increases in the order:  $\text{MnFe}_2\text{O}_4 < \text{NiFe}_2\text{O}_4 < \text{CuFe}_2\text{O}_4 < \text{CoFe}_2\text{O}_4$ , with  $\text{CoFe}_2\text{O}_4$  exhibiting the highest catalytic activity (overpotential,  $\eta = 408$  mV at  $5 \text{ mA cm}^{-2}$ ). Moreover,  $\text{CoFe}_2\text{O}_4$  is the system on which there are more experimental characterization results to compare with, as we will discuss in section 3.2.1.

According to the Wulff-Kaishev theorem [47], for particles deposited on a substrate the surface energy in the Wulff construction has to be rescaled by the adhesion energy. As adhesion stabilizes the system, the rescaled surface energy will be lower and the corresponding facet will increase in size. Analogously, in the case of particles immersed in a chemical environment the adsorption energies of ligand species must be included when rescaling surface energies [39]. Clearly, it is necessary to explore a thorough set of adsorbate configurations to determine the lowest-energy state of the system (corresponding to the resting state under reaction conditions). A variety of adsorption coverages and modes of OH,  $\text{H}_2\text{O}$ ,  $\text{O}_2$  on  $\text{CoFe}_2\text{O}_4$  slab models was therefore investigated to predict Wulff reshaping. Non-stoichiometric but symmetric slabs were built for the three planes [(001), (110), (111)] of  $\text{CoFe}_2\text{O}_4$  inverse spinel, as shown in **Figure 4**.

One important initial observation is that for (110) and (111) the bare-surface termination ended up with a significant distortion of the tetrahedral (under-coordinated) surface Fe atoms upon DFT relaxation. Adsorption of  $\text{O}_2$  molecular species was found to solve this issue. An  $\text{O}_2$  molecule can indeed be put on (110) as a chelate ligand in bridge adsorption mode in two different positions: (a) on tetrahedral Fe-Fe atoms and (b) on octahedral Co-Fe atoms (see **Figure 6a, b**). Note that in **Figure 6** for reasons of clarity the 4 surface lattice oxygens are labeled as O1, O2, O3, O4 along with octahedrally coordinated Co ( $\text{Co}^\ominus$ ) and Fe ( $\text{Fe}^\ominus$ ) atoms and tetrahedrally coordinated Fe ( $\text{Fe}^\oplus$ ) atoms. The addition of  $\text{O}_2$  in a bridge adsorption mode brought about a surface stabilization of -0.28 eV when  $\text{O}_2$  was put on (a) Fe-Fe tetrahedral atoms, whereas in the (b) case a destabilization of +0.07 eV was observed.  $\text{O}_2$  was thus kept on tetrahedral Fe sites for (110) surface adsorption calculations. On (111),  $\text{O}_2$  can be put in bridge between one tetrahedral Fe and one octahedral Co site (see **Figure 6c**). Because of the surface cut, one Fe valence coordination and three Co valence coordination are missing. The

addition of O<sub>2</sub> in a bridge absorption mode has the effect of partially completing the coordination of the upper layer, and indeed we found that O<sub>2</sub> adsorption stabilizes the surface by -0.72 eV. Note however that, while tetrahedral Fe has now completed its four-fold coordination, two coordinated species are still missing for the octahedral Co.

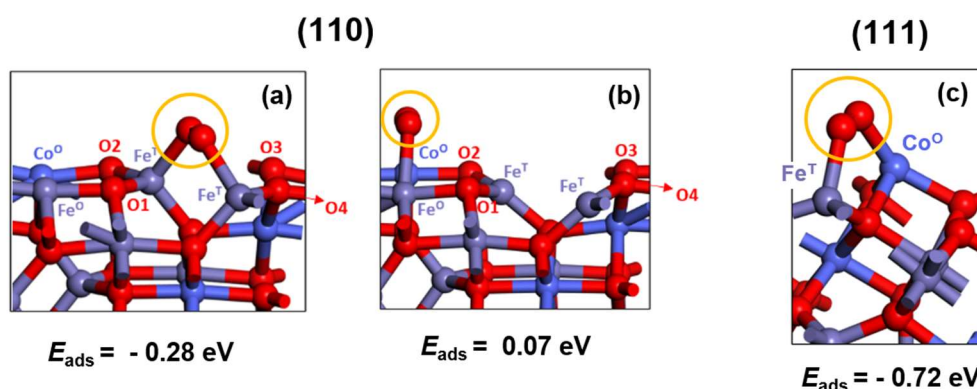


**Figure 6.** O<sub>2</sub> bridged (110) CoFe<sub>2</sub>O<sub>4</sub> surfaces sited on (a) tetrahedral Fe-Fe atoms (b) octahedral Co-Fe atoms. (c) O<sub>2</sub> bridged (111) CoFe<sub>2</sub>O<sub>4</sub> surface sited on octahedral Co – tetrahedral Fe atoms.

Then, as in our previous investigation of the OER catalysis on the (100) facet of CoFe<sub>2</sub>O<sub>4</sub> [23], undissociated water molecules were used to fill in the missing coordination of metal sites on each surface [(001), (110), (111)]. In a further step, the transformation of waters into hydroxyls and hydrogen adatoms via dissociation (\*H<sub>2</sub>O → \*OH + \*H) was considered, and the affinity of \*H<sub>2</sub>O, \*OH, and \*H on the metal sites were predicted by calculating the relative energy of the configurations associated with each coverage pattern. The sampling of several coverage patterns on the catalyst surface allowed us to determine the lowest energy state (i.e., the resting state under reaction conditions) on each of the three facets of CoFe<sub>2</sub>O<sub>4</sub>. Note that, along with stoichiometric coverage (i.e., dissociated and/or un-dissociated water coverage), off stoichiometric patterns with excess hydrogens on surface oxygens, as well as deprotonated surfaces were also considered. The complete set of studied structures is shown and discussed in Figure S2-S6 of the SI. Here, we only show the configurations which we predict as resting states under selected applied potentials, i.e.,  $U = 1.23$  V, 1, 48 V and 1.63 V vs SHE.

After adsorption of reaction intermediates, the surface energies were recalculated by adding adsorption energies ( $E_{ads}$ ) as formalized in Eq.(5). Note that free-energy contributions of reaction species must be added to the DFT energetics and included into adsorption energy as shown in Eq.(4). Finally,  $E_{ads}$  terms including free energy contributions must be divided by the area of adsorbed surfaces for normalization.

$$E_{ads} = E_{system} - [E_{bare} - E_{adsorbates}] \quad (4)$$

$$E_{surf}^{ads} = E_{surf}^{bare} + \frac{E_{ads}}{Area} \quad (5)$$

The lowest energetic structures (i.e., the resting states) resulting from these calculations under different applied potential ( $U = 1.23$  V, 1.48 V, 1.63 V vs SHE) spanning a realistic set of reaction conditions for OER are shown in **Figure 7A,B,C**.

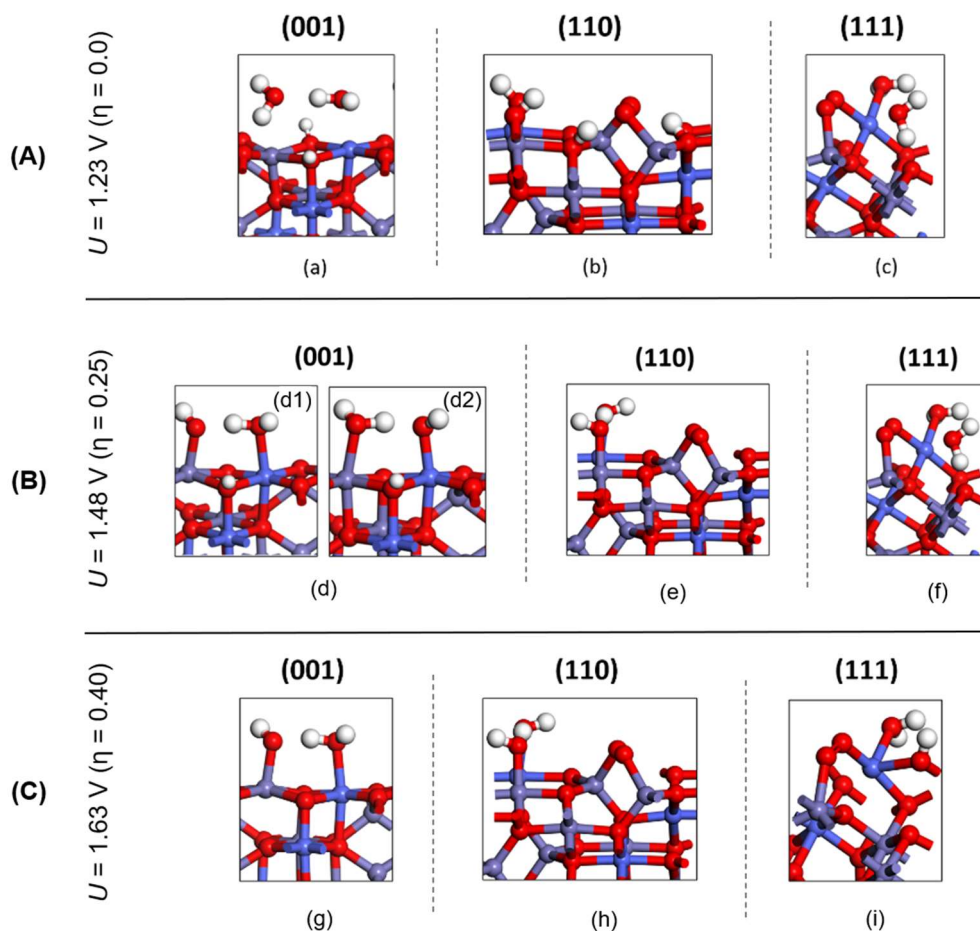


**Figure 7.** Resting state configurations of (001), (110), (111) surfaces of  $\text{CoFe}_2\text{O}_4$  at (A)  $U = 1.23$  V, at (B)  $U = 1.48$  V, (C)  $U = 1.63$  V vs SHE. Oxygen, hydrogen, iron, and cobalt atoms are colored red, white, violet, and indigo-blue, respectively.

The three selected resting states for (001), (110) and (111) under bias  $U = 1.23$  V ( $\eta = 0.0$ ) are shown in panel **Figure 7A**. As for the (001) surface, water adsorption on metal sites along with excess hydrogens on lattice oxygens gave the lowest energy at  $U = 1.23$  V. For (110), the pattern (b) which has an \*OH adsorbed on a bridge region between octahedral Co and Fe atoms along with two hydrogens on lattice oxygens (O1 and O4) gave the lowest energy. For the (111) facet, the state in which two water adsorbates complete the surface Co's missing two octahedral coordination was predicted as the resting state under  $U = 1.23$  V, shown as (c) in **Figure 7A** (see also panel (a) in Figure S7 of the SI).

In **Figure 7B**, four selected resting states for (001), (110) and (111) under bias  $U = 1.48$  V ( $\eta = 0.25$ ) are shown. For the (001) surface there are two resting states corresponding to minimum energy (i.e., dissociated waters on Fe and Co site respectively as shown in Figure S2 (b),(c) of the SI), that are shown in **Figure 7B** (configurations d1, d2). As for (110), the deprotonated pattern with respect to two waters gave the lowest energy at  $U > 1.24$  V among adsorbed patterns. For (111), the same resting state as at  $U = 1.23$  V case (two water coordinated to Co cations) was predicted.

Finally, the resting states under bias  $U = 1.63$  V ( $\eta = 0.40$ ) are shown in **Figure 7C**. For all facets [(001), (110), (111)] of  $\text{CoFe}_2\text{O}_4$ , fully deprotonated surfaces are preferred in this case, providing the lowest energy surfaces at  $U = 1.63$  V.

As a next step, the energies of resting state configurations under  $U = 1.23$  V,  $1.48$  V,  $1.63$  V vs SHE (shown in **Figure 7**) were used to recalculate the surface energies based on Eq.(5), and thus to estimate the Wulff nanoparticle shapes of  $\text{CoFe}_2\text{O}_4$  under the given bias.

In the Table in **Figure 8A**, a comparison of surface energies calculated from non-adsorbed (i.e., bare) surfaces with the surface energies recalculated for adsorbed surfaces under applied potentials

( $U = 1.23 \text{ V}$ ,  $1.48 \text{ V}$ ,  $1.63 \text{ V}$  vs SHE) for  $\text{CoFe}_2\text{O}_4$  inverse spinel is reported. As apparent from this Table, the adsorption process reduces the value of the surface energy for each surface, as expected. The recalculated surface energies for adsorbed facets now increase in the sequence  $\gamma_{111} < \gamma_{001} < \gamma_{110}$ , which is different from the sequence for bare surfaces:  $\gamma_{001} < \gamma_{111} < \gamma_{110}$ . We thus predict an inversion from low-coverage to OER conditions, i.e., we expect to have larger extension of (111) in the Wulff nanoparticle shape under electrochemical conditions. Note that we did not include in our estimates the reaction energy to transform the stoichiometric bare facets to non-stoichiometric covered facets: this reaction involves desorption of Fe cations from the stoichiometric facets, whose energetics is difficult to estimate as it will depend upon environmental conditions (the chemical potential of Fe cations). However, in both free and OER conditions the (110) facets have the highest surface energy (thereof the least stable plane) for spinel surfaces. This is consistent with experimental results, see the discussion below.

Using Eq.(5) and the WulffPack python package [29], the surface energy values in **Figure 8A** were used to obtain Wulff nanoparticle shapes of  $\text{CoFe}_2\text{O}_4$  under applied potentials, and the results are shown in **Figure 8B**. We find that, under OER applied potentials, (111) dominates in all cases with a fraction higher than 90%, while (001) facets occupy less than 10% and (110) facets do not contribute to the Wulff shape. Note that, as the  $U$  value increases, (111) occupies a larger and larger area: at  $U = 1.23 \text{ V}$ , (111) has a fraction of 90.2%, then passing to 92.8% fraction at  $U = 1.48 \text{ V}$ , and ending up to 97.1% at  $U = 1.63 \text{ V}$ . However, these changes as a function of the bias  $U$  are not drastic and may be difficult to be observed experimentally.

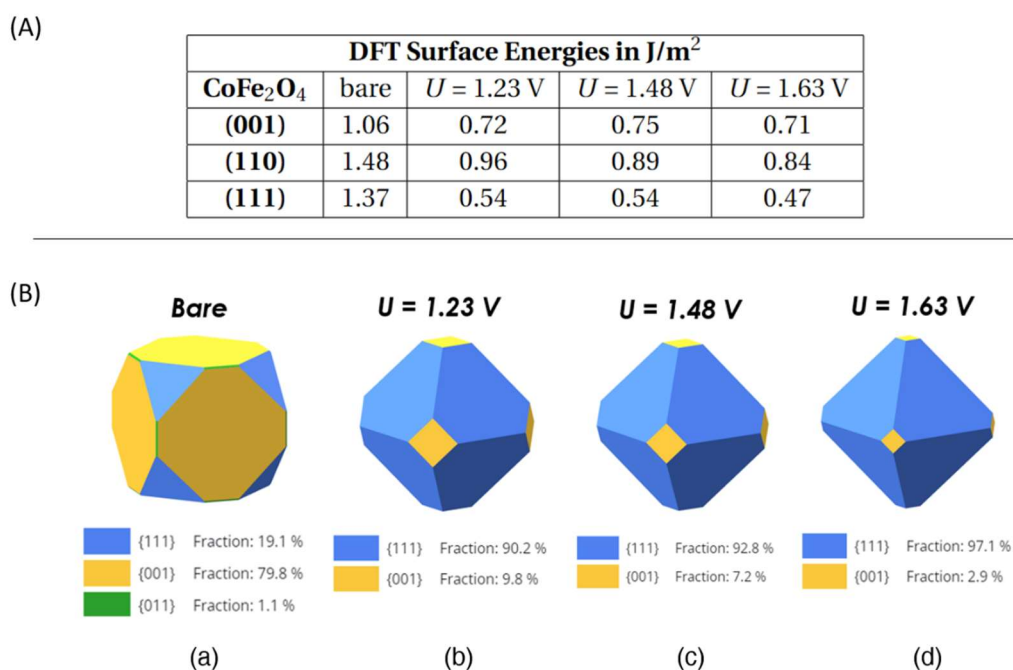


**Figure 8.** (A) Calculated DFT Surface Energies for bare versus adsorbed surfaces of  $\text{CoFe}_2\text{O}_4$  under applied potentials ( $U$ ). (B) Wulff NP shapes of  $\text{CoFe}_2\text{O}_4$  based on (a) bare (i.e., non-adsorbed) terminations, and (b-d) adsorbed/covered surfaces at (b) 1.23 V, (c) 1.48 V and (d) 1.63 V vs SHE, respectively. Conditions of electro-catalysis.

### 3.2.1. Comparison with experiment

In order to validate our theoretical predictions, we now proceed to a comparison with available information from previously published experimental work on spinel oxide nanoparticles in which microscopic characterization of the systems under OER conditions was provided and which therefore lend themselves best to be compared with our Wulff construction predictions. To this purpose, it would be ideal to have microscopy measurements on  $\text{CoFe}_2\text{O}_4$  nanoparticles detected under OER

*operando* conditions. However, to the best of our knowledge there are no examples in the literature of such *operando* experiments. Therefore, we will compare with four experimental studies from the literature in which TEM and HRTEM images of as-prepared  $\text{CoFe}_2\text{O}_4$  nanoparticles or of  $\text{CoFe}_2\text{O}_4$  nanoparticles *after* some cycles of electrochemical treatment have been reported.

Gebrelase *et al.* observed a transformation of the  $\text{CoFe}_2\text{O}_4$  structure by varying and optimizing the ratio of  $\text{CoFe}_2\text{O}_4$  and dopamine contents in a peculiar synthesis recipe [48], reporting a final over-potential of 440 mV at 10 mA/cm<sup>2</sup> for pristine  $\text{CoFe}_2\text{O}_4$ . These  $\text{CoFe}_2\text{O}_4$  samples were prepared via synthesis of spinel oxide nanoparticles by hydrothermal method, addition and polymerization of dopamine in a nanoparticle suspension, finally followed by carbonization via calcination, as described in the original paper [48]. Regarding the  $\text{CoFe}_2\text{O}_4$  nanoparticle shape (their size was 3 to 45 nm in diameter), using HRTEM imaging Gebrelase *et al.* reported an octahedron-like structure for pristine  $\text{CoFe}_2\text{O}_4$  before the OER. The experimental TEM and HRTEM images from their work are reported in **Figure 9a** and **Figure 9b**, and clearly show dominance of the (111) surface, matching the predicted Wulff shapes in **Figures 8b-d**.

Xiang *et al.* used atom probe tomography (APT) to elucidate the evolution of the 3D structure of 10nm-sized  $\text{Co}_2\text{FeO}_4$  and  $\text{CoFe}_2\text{O}_4$  nanoparticles during OER [49]. They observed no significant structural changes in the  $\text{CoFe}_2\text{O}_4$  nanoparticle surface after 100 cycles of OER. After 1000 cycles, they discerned the formation of a  $(\text{Fe}^{\text{III}}, \text{Co}^{\text{III}})\text{O}_3$  phase, speculating that  $\text{Fe}_2\text{O}_3$  forms as the potential increases according to the Fe Pourbaix diagram [50]. Also, they reported an OER activity of pristine  $\text{CoFe}_2\text{O}_4$  with an over-potential of 432 mV at 10 mA/cm<sup>2</sup> (1.66 V vs RHE), and reported TEM images of  $\text{CoFe}_2\text{O}_4$  nanoparticles that are reported in **Figure 9c**. Comparing microscopy images of pristine  $\text{CoFe}_2\text{O}_4$  nanoparticles in Ref. [49] with our calculated nanoparticles at  $U=1.63$  V in **Figure 8c**, one notice that the TEM images often show a more spherical shape than that predicted by the present study. However, in the experiments one can find more faceted nanoparticles as well: for example, the nanoparticle enclosed in a yellow circle in **Figure 9c** exhibits (111) planes due to its prismatic/sharp edges, and compares very favorably with our predictions.

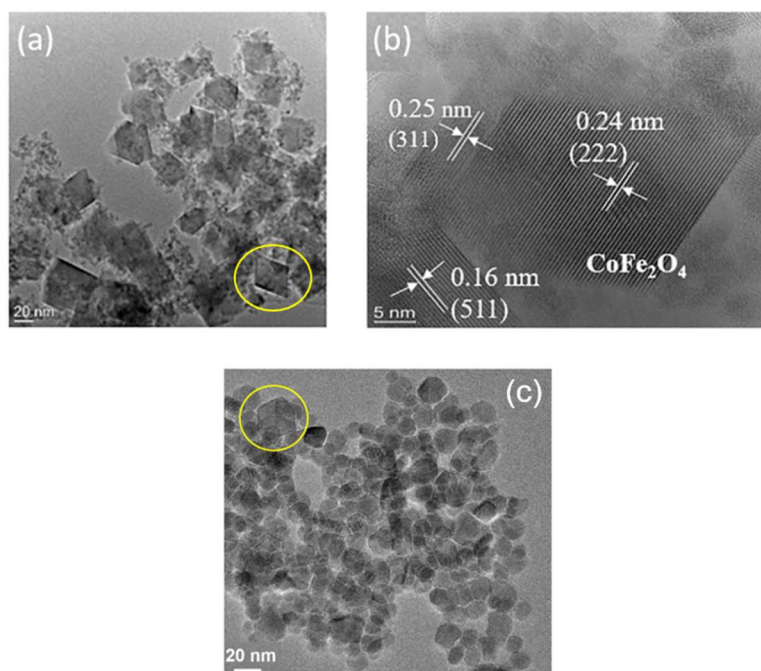


**Figure 9.** (a) TEM image of pristine  $\text{CoFe}_2\text{O}_4$  nanoparticles. (b) HRTEM images with and lattice fringe analyses of pristine  $\text{CoFe}_2\text{O}_4$ . (a-b) Figures adapted from Ref [48]. Copyright@ Elsevier 2022 (c) TEM image of the pristine  $\text{CoFe}_2\text{O}_4$  nanoparticles in Xiang *et al.* work. Figure adapted from Ref [49]. Copyright@ Springer Nature 2022.

Arrassi *et al.* analyzed 4 nm-sized  $\text{CoFe}_2\text{O}_4$  spinel nanoparticles, and showed that these particles retain their size and crystal structure after OER as observed via area electron diffraction measurements (SAED) [51].  $\text{CoFe}_2\text{O}_4$  was tested in its intrinsic catalytic response without binders or additives and OER was recorded at a potential of 1.86 V vs RHE. They also detected (111) faceting in nanoparticles with SAED analysis before and after electrochemistry experiments, and observed no structural changes after OER, in agreement with theoretical calculations under a wide range of bias in the present study.

Finally, in the study of Kargar *et al.* [52], the sample morphology and material composition of  $\text{CoFe}_2\text{O}_4$  nanoparticles on carbon fiber papers (NPs-on-CFPs) were examined after long-term stability testing under OER. After more than 15 hours of long cycle testing (>1000 cycles), the sample was thoroughly examined using SEM imaging, XRD and elemental mapping analyses – we refer to the original work [52] for the details for the experimental analysis. Similarly to previous studies, they concluded that the morphology of  $\text{CoFe}_2\text{O}_4$  NPs-on-CFP did not change significantly, and the samples showed long term stability without any morphological or compositional modifications.

### 3.2.1. Effect of oxygen pressure on nanoparticle shape

We noted above that  $\text{O}_2$  adsorption has a role in stabilizing the (110) and (111) surfaces of  $\text{CoFe}_2\text{O}_4$ . The physical reason of this unusually high adsorption energy lies in the *charge state of the  $\text{O}_2$  molecule*. We have performed a Bader analysis of the configuration depicted in **Figure 6c**, which exhibit the highest  $\text{O}_2$  desorption energy, and found that each oxygen atom bears a charge of -0.4 e, for a total of a charge of -0.8 e for the  $\text{O}_2$  molecule. For reference, the oxygen anions in the bulk, which formally correspond to doubly negatively charged species, bear a Bader charge of -1.2 e. The adsorbed  $\text{O}_2$  thus corresponds essentially to a superoxide anion,  $\text{O}_2^-$ . A perusal of bond distances confirms this analysis: the O-O distance in the configuration depicted in **Figure 6c** is 1.36 Å, to be compared with a distance of 1.22 Å for the (neutral)  $\text{O}_2$  molecule, 1.35 Å in the (singly negative) superoxide  $\text{LiO}_2$  molecule, and 1.58 Å in the (doubly negative) peroxide  $\text{Li}_2\text{O}_2$ , respectively.

Given this sizeable adsorption energy, in this section we will explore whether it is possible to change the nanoparticle shape by controlling the  $\text{O}_2$  pressure. We use standard thermodynamics to calculate the Gibbs free energy of  $\text{O}_2$  in actual conditions ( $\Delta G$ ), which is related to the Gibbs free energy in the standard state ( $\Delta G^\circ$ ) by the relationship:

$$\Delta G = \Delta G^\circ + RT \ln Q_r \quad (6)$$

Here,  $Q_r$  is the reaction quotient which allows one to estimate the changes (i.e. temperature, concentration, pressure etc.) under non-standard conditions. The effect of pressure was therefore included by adding the last term in Eq.(6) to the adsorption energy ( $E_{\text{ads}}$ ) calculations, see Eq.(5) for (110) and (111) facets. We focused on a bias of  $U = 1.48$  V (also considering 1.63 V in the SI) and investigated both increasing oxygen pressure up to 30 atm (1 atm, 5 atm, 15 atm and 30 atm), and also decreasing oxygen pressure down to  $10^{-4}$  atm. Note that the (001) surface energy was kept at 0.75 J/m<sup>2</sup> and 0.71 J/m<sup>2</sup> at  $U = 1.48$  V and 1.63 V, respectively, as this facet does not carry  $\text{O}_2$  in its resting state. Rescaled surface energies and Wulff constructions are reported in **Figure 10** at  $U = 1.48$  V, as this bias is presently the optimal target of only 0.25 V over-potential and is considered as the one realistically closest to the minimum voltage necessary for water electrolysis (1.23 V). Results at  $U = 1.63$  V are additionally shown in Figure S8 of the SI. **Figure 10** clearly demonstrates that changing the oxygen pressure has a dramatic effect on the surface energies and then Wulff shape, with the (111) facet favored at high  $\text{O}_2$  pressure, and the (100) facet favored at low  $\text{O}_2$  pressure. In contrast, it can be noted that, despite these dramatic changes, the (110) surface energies are still too high to make the contribution of this facet significant compared to other surfaces of  $\text{CoFe}_2\text{O}_4$ . Under 15 to 30 atm of  $\text{O}_2$  pressure at  $U = 1.43$  V - 1.63 V, the surface energies of (110) were computed lower than (001), nonetheless the (111) surface energy in parallel also decreases significantly, so that eventually we predict a full fraction 100% of (111) in a purely octahedron shape (see **Figure 10e**). At the opposite, when the  $\text{O}_2$  pressure is decreased down to 0.5 atm, the surface energy of (111) approaches the value of (001), and the (001) area on the nanoparticles gradually increases. Dramatically, when the  $\text{O}_2$

pressure is reduced to very low values of  $10^{-4}$  atm, the nanoparticle surfaces become a full fraction 100% of (001) with a purely cube shape, as shown in **Figure 10a**.

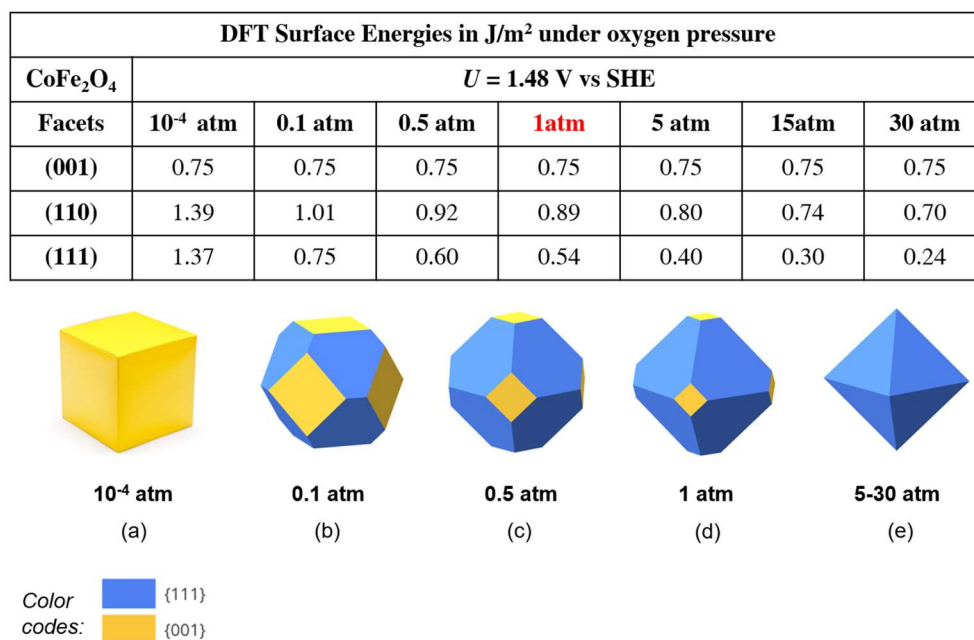


**Figure 10.** Calculated DFT Surface Energies with oxygen pressure ( $10^{-4}$  to 30 atm) on (001), (110) and (111) surfaces of CoFe<sub>2</sub>O<sub>4</sub> under applied potential  $U = 1.48 \text{ V vs SHE}$  (above). Wulff NP shapes of CoFe<sub>2</sub>O<sub>4</sub> under  $U = 1.48 \text{ V}$ , ranged from  $10^{-4}$  atm (a) to 30 atm (e). Color codes: blue for (111), yellow for (001) facets. Conditions of electro-catalysis.

In the light of above findings, we conclude that increasing O<sub>2</sub> pressure might poison the catalyst in the OER process. Indeed, increasing O<sub>2</sub> pressure increases the size of the higher-index facets, i.e., (111) and (110), at the expense of the low-index (001) facet, whereas decreasing O<sub>2</sub> pressure has the opposite effect. Now, although the (111) facets is catalytically active [24-26], its activity can be poisoned by the adsorption of the O<sub>2</sub> reaction product, whereas the catalytic activity of the (001) facet may be higher and should not be affected by O<sub>2</sub> pressure [23]. These findings thus suggest to work experimentally at as low O<sub>2</sub> pressure as possible in order to maximize OER catalytic activity of CoFe<sub>2</sub>O<sub>4</sub> – in general, spinel oxide – materials. According to our DFT modeling, in fact, the (001) facet should completely dominate the nanoparticle shape at an O<sub>2</sub> pressure of  $10^{-4}$  atm.

#### 4. Conclusions

Our aim in this work is to predict and elucidate nanoparticle shape under diverse environments, for both validation and production purposes, to provide ground for *operando* monitoring of these promising catalysts and compare with available experimental data. We are especially interested in predicting from first-principles simulations nanoparticle shapes *under OER electrochemical conditions*, that to the best of our knowledge has not been attempted thus far. To achieve this goal, we systematically investigated the surface structures of the low-index facets [(001), (110) and (111)] of a set of spinel oxides (NiFe<sub>2</sub>O<sub>4</sub>, CoFe<sub>2</sub>O<sub>4</sub>, NiCo<sub>2</sub>O<sub>4</sub>, ZnCo<sub>2</sub>O<sub>4</sub>) using periodic DFT+U calculations under two different sets of conditions, corresponding to the two possible catalytic applications of these systems: (i) as bare surfaces under vacuum or low-coverage high-temperature conditions typical of chemical looping or oxidation reactions [9-12], and (ii) as adsorbate-covered facets under OER (limiting to the CoFe<sub>2</sub>O<sub>4</sub> system as a paradigmatic example) [20-23]. The calculated surface energies were then used in the Wulff construction to predict the equilibrium nanoparticle shapes of spinel oxides under the different environmental conditions.

For bare surfaces under vacuum, regardless of the nature of the alien metal in the mixed iron and cobalt spinels, we found that the abundance of the (110) faces is always low, and that (001) facets

dominates the nanoparticle shapes, in agreement with experiment and a previous systematic study [8].

CoFe<sub>2</sub>O<sub>4</sub>, a promising non-critical-material candidate for OER/AEMWE catalysis, was then selected to comprehensively study the adsorbate-covered resting state surface structures of low index surfaces [(001), (110) and (111)] *under OER conditions*, exploiting results of a previous study on OER catalysis [23].

First, we found that under OER the ordering of surface energies changes with respect to bare systems from  $\gamma_{001} < \gamma_{111} < \gamma_{110}$  to  $\gamma_{111} < \gamma_{001} < \gamma_{110}$  under a wide range of realistic applied potentials. Then, building the optimal nanoparticle shape via the Wulff construction, we predict that CoFe<sub>2</sub>O<sub>4</sub> exhibit dominant (111) facets up to 1.63 V bias vs SHE, in fair agreement with experimental TEM and HRTEM observations.

Second, we investigated the effect of oxygen pressure, to the best of our knowledge here for the first time. We predict that, upon O<sub>2</sub> adsorption, a stabilization takes place for the (110) and especially the (111) surfaces of CoFe<sub>2</sub>O<sub>4</sub>. We rationalize this prediction in terms of the formation of a strongly adsorbed superoxide-like species on (110) and (111). Dramatic changes in the Wulff shapes are predicted: at high O<sub>2</sub> pressure, the (111) facet will dominate in a purely octahedron nanoparticle shape, whereas, at low O<sub>2</sub> pressure, the (001) will eventually become dominant, to achieve a purely cubic nanoparticle shape. Considering that (001) is a catalytically active facet whose activity does not depend on O<sub>2</sub> pressure [23], whereas (111) is catalytically active [24-26], but may be poisoned by the adsorption of the reaction product, this implies that O<sub>2</sub> can poison the catalysts, and ideal OER conditions may correspond to as low O<sub>2</sub> pressure as possible.

In perspective, we underline the importance of investigating computationally nanoparticle reshaping of spinel oxides under operating conditions together with experimental *operando* characterization of these systems. This should open the way to cross-validation between theory and experiment, that should lead to a deeper understanding and then eventually to a rational design of much-needed more efficient and sustainable optimized catalysts in both oxidation and OER catalysis. In perspective, it will also be very interesting to further extend our approach by including defects such as oxygen vacancies in the surface energetics [53], or more complex, composite architectures [54,55].

**Supplementary Materials:** The following supporting information can be downloaded at: Preprints.org, Slab Models for Surface Energy Calculations, Surface Coverage for [(001), (110), (111)] planes of CoFe<sub>2</sub>O<sub>4</sub>, Wulff shapes as a function of oxygen pressure.

**Author Contributions:** Conceptualization, A.F.; Methodology, A.F. and L.S.; Validation, O.N.A.; Formal Analysis, A.F. and O.N.A.; Investigation, L.S. and O.N.A.; Resources, A.F.; Data Curation, O.N.A.; Writing – Original Draft Preparation, O.N.A.; Writing – Review & Editing, A.F., L.S., and O.N.A.; Visualization, O.N.A.; Supervision, A.F. and L.S.; Funding Acquisition, A.F.

**Funding:** This research was funded by European Union's Horizon 2020 Research and Innovation programme under the Marie Skłodowska-Curie Actions-Innovative Training Networks (MSCA-ITN) Grant Agreement 813748 (BIKE project).

**Data Availability Statement:** The data presented in this study are available on request from the corresponding author.

**Acknowledgments:** Financial support from the European Union's Horizon 2020 Research and Innovation programme under the Marie Skłodowska-Curie Actions-Innovative Training Networks (MSCA-ITN) Grant Agreement 813748 (BIKE project) is gratefully acknowledged. Computational support from CINECA supercomputing centre within the ISCRA programme is also gratefully acknowledged.

**Conflicts of Interest:** The authors declare no competing financial interest.

## References

1. Barmparis, G. D.; Lodziana, Z.; Lopez, N.; Remediakis, I. N. Nanoparticle Shapes by Using Wulff Constructions and First-Principles Calculations. *Beilstein J. Nanotech.* **2015**, *6*, 361–368. <https://doi.org/10.3762/bjnano.6.35>.

- Sun, Y.; Xia, Y. Shape-controlled synthesis of gold and silver nanoparticles. *Science*. **2002**, *298*, 2176-2179. <https://doi.org/10.1126/science.1077229>.
- Wulff, G. Zur Frage der Geschwindigkeit des Wachstums und der Auflösung der Krystallflächen, *Zeitschrift für Kristallographie - Crystalline Materials*. **1901**, *34*, 449-530. <https://doi.org/10.1524/zkri.1901.34.1.449>
- Gibbs, J. W. On the Equilibrium of Heterogeneous Substances. *Am. J. Science* **1878**, *s3-16*, 441-458. <https://doi.org/10.2475/ajs.s3-16.96.441>.
- Honkala, K.; Hellman, A.; Remediakis, I. N.; Logadottir, A.; Carlsson, A.; Dahl, S.; Christensen, C. H.; Nørskov, J. K. Ammonia Synthesis from First-Principles Calculations. *Science* **2005**, *307*, 555-558. <https://doi.org/10.1126/science.1106435>.
- Vilé, G.; Baudouin, D.; Remediakis, I. N.; Copéret, C.; López, N.; Pérez-Ramírez, J. Silver Nanoparticles for Olefin Production: New Insights into the Mechanistic Description of Propyne Hydrogenation. *ChemCatChem*. **2013**, *5*, 3750-3759. <https://doi.org/10.1002/cctc.201300569>.
- Barnparis, G. D.; Remediakis, I. N. Dependence on CO Adsorption of the Shapes of Multifaceted Gold Nanoparticles: A Density Functional Theory. *Phys. Rev. B*. **2012**, *86*, 085457. <https://doi.org/10.1103/physrevb.86.085457>.
- Zasada, F.; Gryboś, J.; Indyka, P.; Piskorz, W.; Kaczmarczyk, J.; Sojka, Z. Surface Structure and Morphology of M[CoM']O<sub>4</sub> (M = Mg, Zn, Fe, Co and M' = Ni, Al, Mn, Co) Spinel Nanocrystals—DFT+U and TEM Screening Investigations. *J. Phys. Chem. C* **2014**, *118*, 19085-19097. <https://doi.org/10.1021/jp503737p>.
- Zhu, M.; Wachs, I. E. Iron-Based Catalysts for the High-Temperature Water-Gas Shift (HT-WGS) Reaction: A Review. *ACS Catalysis* **2016**, *6* (2), 722-732.
- Villa, R. Ni Based Mixed Oxide Materials for CH<sub>4</sub> Oxidation under Redox Cycle Conditions. *Journal of Molecular Catalysis A: Chemical* **2003**, *204-205*, 637-646. [https://doi.org/10.1016/s1381-1169\(03\)00346-7](https://doi.org/10.1016/s1381-1169(03)00346-7).
- Anke, S.; Bendt, G.; Ilya Sinev; Hamidreza Hajiyani; Antoni, H.; Ioannis Zegkinoglou; Hyo Sang Jeon; Rossitza Pentcheva; Beatriz Roldan Cuenya; Schulz, S.; Muhler, M. Selective 2-Propanol Oxidation over Unsupported Co<sub>3</sub>O<sub>4</sub> Spinel Nanoparticles: Mechanistic Insights into Aerobic Oxidation of Alcohols. *ACS Catalysis* **2019**, *9* (7), 5974-5985. <https://doi.org/10.1021/acscatal.9b01048>.
- Scheffe, J. R.; Allendorf, M. D.; Coker, E. N.; Jacobs, B. W.; McDaniel, A. H.; Weimer, A. W. Hydrogen Production via Chemical Looping Redox Cycles Using Atomic Layer Deposition-Synthesized Iron Oxide and Cobalt Ferrites. *Chemistry of Materials* **2011**, *23* (8), 2030-2038. <https://doi.org/10.1021/cm103622e>.
- Chmielewski, A.; Meng, J.; Zhu, B.; Gao, Y.; Guesmi, H.; Prunier, H.; Alloyeau, D.; Wang, G.; Louis, C.; Delannoy, L.; Afanasiev, P.; Ricolleau, C.; Nelayah, J. Reshaping Dynamics of Gold Nanoparticles under H<sub>2</sub> and O<sub>2</sub> at Atmospheric Pressure. *ACS Nano*. **2019**, *13*, 2024-2033. <https://doi.org/10.1021/acsnano.8b08530>.
- West, P. S.; Johnston, R. L.; Barcaro, G.; Fortunelli, A. The Effect of CO and H Chemisorption on the Chemical Ordering of Bimetallic Clusters. *J. Phys. Chem. C* **2010**, *114*, 19678-19686. <https://doi.org/10.1021/jp108387x>.
- Geysermans, P.; Finocchi, F.; Goniakowski, J.; Hacquart, R.; Jupille, J. Combination of (100), (110) and (111) Facets in MgO Crystals Shapes from Dry to Wet Environment. *Phys. Chem. Chem. Phys.* **2009**, *11*, 2228-2233. <https://doi.org/10.1039/b812376d>.
- Molina, L. M.; Lee, S.; Sell, K.; Barcaro, G.; Fortunelli, A.; Lee, B.; Seifert, S.; Winans, R. E.; Elam, J. W.; Pellin, M. J. Size-Dependent Selectivity and Activity of Silver Nanoclusters in the Partial Oxidation of Propylene to Propylene Oxide and Acrolein: A Joint Experimental and Theoretical Study. *Catal. Today* **2011**, *160*, 116-130. <https://doi.org/10.1016/j.cattod.2010.08.022>
- An, Q.; McDonald, M.; Fortunelli, A.; Goddard, W. A. Controlling the Shapes of Nanoparticles by Dopant-Induced Enhancement of Chemisorption and Catalytic Activity: Application to Fe-Based Ammonia Synthesis. *ACS Nano* **2020**, *15*, 1675-1684. <https://doi.org/10.1021/acsnano.0c09346>.
- Akbashev, A. R. Electrocatalysis Goes Nuts. *ACS Catal.* **2022**, *12*, 4296-4301. <https://doi.org/10.1021/acscatal.2c00123>.
- Suen, N.-T.; Hung, S.-F.; Quan, Q.; Zhang, N.; Xu, Y.-J.; Chen, H. M. Electrocatalysis for the Oxygen Evolution Reaction: Recent Development and Future Perspectives. *Chem. Soc. Rev.* **2017**, *46*, 337-365. <https://doi.org/10.1039/c6cs00328a>.
- Zhao, Q.; Yan, Z.; Chen, C.; Chen, J. Spinels: Controlled Preparation, Oxygen Reduction/Evolution Reaction Application, and Beyond. *Chemical Reviews* **2017**, *117* (15), 10121-10211. <https://doi.org/10.1021/acs.chemrev.7b00051>.
- Pandiarajan, T.; John Berchmans, L.; Ravichandran, S. Fabrication of Spinel Ferrite Based Alkaline Anion Exchange Membrane Water Electrolysers for Hydrogen Production. *RSC Adv.* **2015**, *5*, 34100-34108. <https://doi.org/10.1039/C5RA01123I>
- Cheng, F.; Shen, J.; Peng, B.; Pan, Y.; Tao, Z.; Chen, J. Rapid Room-Temperature Synthesis of Nanocrystalline Spinels as Oxygen Reduction and Evolution Electrocatalysts. *Nature Chem.* **2010**, *3*, 79-84. <https://doi.org/10.1038/nchem.931>

23. Avci, Ö. N.; Sementa, L.; Fortunelli, A. Mechanisms of the Oxygen Evolution Reaction on NiFe<sub>2</sub>O<sub>4</sub> and CoFe<sub>2</sub>O<sub>4</sub> Inverse-Spinel Oxides. *ACS Catal.* **2022**, *12*, 9058–9073. <https://doi.org/10.1021/acscatal.2c01534>
24. Zhang, Y.; Zhang, G.; Li, W.; Li, X.; Uchiyama, K.; Chen, C. Enhancing Oxygen Reduction Activity by Exposing (111) Facets of CoFe<sub>2</sub>O<sub>4</sub> Octahedron on Graphene. *Chemistry Select* **2017**, *2*, 9878–9881. <https://doi.org/10.1002/slct.201701892>.
25. Chen, Z.; Cronawitter, C. X.; Koel, B. Facet-dependent activity and stability of Co<sub>3</sub>O<sub>4</sub> nanocrystals towards the oxygen evolution reaction. *Phys. Chem. Chem. Phys.* **2015**, *17*, 29387–29393. <https://doi.org/10.1039/C5CP02876K>.
26. Li, A.; Kong, S.; Guo, C.; Ooka, H.; Adachi, K.; Hashizume, D.; Jiang, Q.; Han, H.; Xiao, J.; Nakamura, R. Enhancing the stability of cobalt spinel oxide towards sustainable oxygen evolution in acid. *Nature Catal.* **2022**, *5*, 109–118. <https://doi.org/10.1038/s41929-021-00732-9>.
27. Tolba, S. A.; Gameel, K. M.; Ali, B. A.; Almossalami, H. A.; Allam, N. K. The DFT+U: Approaches, Accuracy, and Applications. *Density Functional Calculations - Recent Progresses of Theory and Application*, in *Density Functional Calculations*. Yang, G. ed. **2018**. <https://doi.org/10.5772/intechopen.72020>.
28. Vanderbilt, D. Soft Self-Consistent Pseudopotentials in a Generalized Eigenvalue Formalism. *Phys. Rev. B.* **1990**, *41*, 7892–7895. <https://doi.org/10.1103/PhysRevB.41.7892>
29. Giannozzi, P.; Baroni, S.; Bonini, N.; Calandra, M.; Car, R.; Cavazzoni, C.; Ceresoli, D.; Chiarotti, G. L.; Cococcioni, M.; Dabo, I.; Dal Corso, A.; de Gironcoli, S.; Fabris, S.; Fratesi, G.; Gebauer, R.; Gerstmann, U.; Gougoussis, C.; Kokalj, A.; Lazzeri, M.; Martin-Samos, L.; Marzari, N.; Mauri, F.; Mazzarello, R.; Paolini, S.; Pasquarello, A.; Paulatto, L.; Sbraccia, C.; Scandolo, S.; Sclauzero, G.; Seitsonen, A. P.; Smogunov, A.; Umari, P.; Wentzcovitch, R. M. J. QUANTUM ESPRESSO: a modular and open-source software project for quantum simulations of materials. *Phys.: Condens. Matter.* **2009**, *21*, 395502. <https://doi.org/10.1088/0953-8984/21/39/395502>
30. Perdew, J. P.; Burke, K.; Ernzerhof, M. Generalized Gradient Approximation Made Simple. *Phys. Rev. Lett.* **1996**, *77*, 3865–3868. <https://doi.org/10.1103/PhysRevLett.77.3865>.
31. Shi, X.; Bernasek, S. L.; Selloni, A. Formation, Electronic Structure, and Defects of Ni Substituted Spinel Cobalt Oxide: A DFT+U Study. *J. Phys. Chem. C* **2016**, *120*, 14892–14898. <https://doi.org/10.1021/acs.jpcc.6b03096>.
32. Selcuk, S.; Selloni, A. DFT+U Study of the Surface Structure and Stability of Co<sub>3</sub>O<sub>4</sub>(110): Dependence on U. *J. Phys. Chem. C* **2015**, *119*, 9973–9979. <https://doi.org/10.1021/acs.jpcc.5b02298>.
33. Wang, L.; Maxisch, T.; Ceder, G. Oxidation Energies of Transition Metal Oxides within TheGGA+Uframework. *Phys. Rev. B* **2006**, *73*, 195107. <https://doi.org/10.1103/physrevb.73.195107>.
34. Rahm, J.; Erhart, P. WulffPack: A Python Package for Wulff Constructions. *J. Open Source Software.* **2020**, *5*, 1944.
35. Wen, X. L.; Chen, Z.; Liu, E. H.; Lin, X. Structural and Magnetic Characterization of ZnCo<sub>2</sub>O<sub>4</sub> Thin Film Prepared by Pulsed Laser Deposition. *Appl. Surf. Sci.* **2015**, *357*, 1212–1216. <https://doi.org/10.1016/j.apsusc.2015.09.152>.
36. Chen, Z.; Wen, X. L.; Niu, L. W.; Duan, M.; Zhang, Y. J.; Dong, X. L.; Zhang, R. L.; Chen, C. L. Transport and Magnetic Properties of ZnCo<sub>2</sub>O<sub>4</sub>/Si Heterostructures Grown by Radio Frequency Magnetron Sputtering. *Thin Solid Films.* **2014**, *573*, 90–94. <https://doi.org/10.1016/j.tsf.2014.10.103>.
37. Montoya, A.; Haynes, B. S. Periodic Density Functional Study of Co<sub>3</sub>O<sub>4</sub> Surfaces. *Chem. Phys. Lett.* **2011**, *502*, 63–68. <https://doi.org/10.1016/j.cplett.2010.12.015>.
38. Zasada, F.; Piskorz, W.; Stelmachowski, P.; Kotarba, A.; Paul, J.-F.; Płociński, T.; Kurzydłowski, K. J.; Sojka, Z. Periodic DFT and HR-STEM Studies of Surface Structure and Morphology of Cobalt Spinel Nanocrystals. Retrieving 3D Shapes from 2D Images. *J. Phys. Chem. C* **2011**, *115*, 6423–6432. <https://doi.org/10.1021/jp200581s>.
39. Chmielewski, A.; Meng, J.; Zhu, B.; Gao, Y.; Guesmi, H.; Prunier, H.; Alloyeau, D.; Wang, G.; Louis, C.; Delannoy, L.; Afanasiev, P.; Ricolleau, C.; Nelayah, J. Reshaping Dynamics of Gold Nanoparticles under H<sub>2</sub> and O<sub>2</sub> at Atmospheric Pressure. *ACS Nano.* **2019**, *13*, 2024–2033. <https://doi.org/10.1021/acsnano.8b08530>.
40. Li, Y.-F.; Selloni, A. Mechanism and Activity of Water Oxidation on Selected Surfaces of Pure and Fe-Doped NiOx. *ACS Catal.* **2014**, *4*, 1148–1153. <https://doi.org/10.1021/cs401245q>.
41. Li, Y.-F.; Liu, Z.-P.; Liu, L.; Gao, W. Mechanism and Activity of Photocatalytic Oxygen Evolution on Titania Anatase in Aqueous Surroundings. *J. Am. Chem. Soc.* **2010**, *132*, 13008–13015. <https://doi.org/10.1021/ja105340b>.
42. Lide, D. R. CRC Handbook of Chemistry and Physics, 84th ed.; Ed.; CRC Press: Boca Raton, FL, 2003.
43. Nørskov, J. K.; Rossmeisl, J.; Logadottir, A.; Lindqvist, L.; Kitchin, J. R.; Bligaard, T.; Jónsson, H. Origin of the Overpotential for Oxygen Reduction at a Fuel-Cell Cathode. *J. Phys. Chem. B* **2004**, *108* (46), 17886–17892. <https://doi.org/10.1021/jp047349j>.
44. Gong, M.; Dai, H. A Mini Review of NiFe-Based Materials as Highly Active Oxygen Evolution Reaction Electrocatalysts. *Nano Res.* **2014**, *8*, 23–39. <https://doi.org/10.1007/s12274-014-0591-z>.

45. Xiao, H.; Shin, H.; Goddard, W. A. Synergy between Fe and Ni in the Optimal Performance of (Ni,Fe)OOH Catalysts for the Oxygen Evolution Reaction. *Proc. Nat. Ac. Sci.* **2018**, *115*, 5872–5877. <https://doi.org/10.1073/pnas.1722034115>.
46. Li, M.; Xiong, Y.; Liu, X.; Bo, X.; Zhang, Y.; Han, C.; Guo, L. Facile Synthesis of Electrospun MFe<sub>2</sub>O<sub>4</sub> (M = Co, Ni, Cu, Mn) Spinel Nanofibers with Excellent Electrocatalytic Properties for Oxygen Evolution and Hydrogen Peroxide Reduction. *Nanoscale*. **2015**, *7* (19), 8920–8930. <https://doi.org/10.1039/c4nr07243j>.
47. Müller, P.; Kern, R. Equilibrium Nano-Shape Changes Induced by Epitaxial Stress (Generalised Wulff-Kaishew Theorem). *Surf. Sci.* **2000**, *457*, 229–253. [https://doi.org/10.1016/s0039-6028\(00\)00371-x](https://doi.org/10.1016/s0039-6028(00)00371-x).
48. Gebreslase, G. A.; Martínez-Huerta, M. V.; Sebastián, D.; Lázaro, M. J. Transformation of CoFe<sub>2</sub>O<sub>4</sub> Spinel Structure into Active and Robust CoFe Alloy/N-Doped Carbon Electrocatalyst for Oxygen Evolution Reaction. *J. Colloid Interface Sci.* **2022**, *625*, 70–82. <https://doi.org/10.1016/j.jcis.2022.06.005>.
49. Xiang, W.; Yang, N.; Li, X.; Linnemann, J.; Hagemann, U.; Ruediger, O.; Heidelmann, M.; Falk, T.; Aramini, M.; DeBeer, S.; Muhler, M.; Tschulik, K.; Li, T. 3D Atomic-Scale Imaging of Mixed Co-Fe Spinel Oxide Nanoparticles during Oxygen Evolution Reaction. *Nature Commun.* **2022**, *13*, 179, <https://doi.org/10.1038/s41467-021-27788-2>.
50. Beverskog, B.; Puigdomenech, I. Revised Pourbaix Diagrams for Iron at 25–300 °C. *Corrosion Sci.* **1996**, *38*, 2121–2135. [https://doi.org/10.1016/s0010-938x\(96\)00067-4](https://doi.org/10.1016/s0010-938x(96)00067-4).
51. El Arrassi, A.; Liu, Z.; Evers, M. V.; Blanc, N.; Bendt, G.; Saddeler, S.; Tetzlaff, D.; Pohl, D.; Damm, C.; Schulz, S.; Tschulik, K. Correction to “Intrinsic Activity of Oxygen Evolution Catalysts Probed at Single CoFe<sub>2</sub>O<sub>4</sub> Nanoparticles.” *J. Am. Chem. Soc.* **2019**, *141*, 10565–10565. <https://doi.org/10.1021/jacs.9b06330>.
52. Kargar, A.; Yavuz, S.; Kim, T. K.; Liu, C.-H.; Kuru, C.; Rustomji, C. S.; Jin, S.; Bandaru, P. R. Solution-Processed CoFe<sub>2</sub>O<sub>4</sub> Nanoparticles on 3D Carbon Fiber Papers for Durable Oxygen Evolution Reaction. *ACS Appl. Mater. Interfaces* **2015**, *7*, 17851–17856. <https://doi.org/10.1021/acsami.5b04270>.
53. Fan, Y.; Zhang, J.; Luo, K.; Zhou, X.; Zhao, J.; Bao, W.; Su, H.; Wang, N.; Zhang, P.; Luo, Z. Oxygen defect engineering on low-crystalline iron(III) oxyhydroxide as a highly efficient electrocatalyst for water oxidation. *Inorg. Chem. Front.* **2024**, *11*, 114–122. <https://doi.org/10.1039/d3qi02043f>.
54. Zhang, L.-C.; Wang, M.-Q.; Chen, H.; Liu, H.; Wang, Y.; Zhang, L.-Z.; Hou, G.-R.; Bao, S.-H. Hierarchical growth of vertically standing Fe<sub>3</sub>O<sub>4</sub>-FeSe/CoSe<sub>2</sub> nano-array for high effective oxygen evolution reaction. *Mater. Res. Bull.* **2020**, *122*, 110680. <https://doi.org/10.1016/j.materresbull.2019.110680>.
55. Park, J.-W.; Ju, Y.-W. Evaluation of Bi-Functional Electrochemical Catalytic Activity of Co<sub>3</sub>O<sub>4</sub>-CoFe<sub>2</sub>O<sub>4</sub> Composite Spinel Oxide. *Energies* **2023**, *16*, 173. <https://doi.org/10.3390/en16010173>.

**Disclaimer/Publisher’s Note:** The statements, opinions and data contained in all publications are solely those of the individual author(s) and contributor(s) and not of MDPI and/or the editor(s). MDPI and/or the editor(s) disclaim responsibility for any injury to people or property resulting from any ideas, methods, instructions or products referred to in the content.